HAL
open science

Energy budget and mechanisms of cold ion heating in asymmetric magnetic reconnection

Sergio Toledo-Redondo, M. André, Y. V. Khotyaintsev, Benoit Lavraud, A. Vaivads, Daniel B. Graham, Wenya Li, Denise Perrone, Stephen Fuselier, D. J. Gershman, et al.

To cite this version:

Sergio Toledo-Redondo, M. André, Y. V. Khotyaintsev, Benoit Lavraud, A. Vaivads, et al.. Energy budget and mechanisms of cold ion heating in asymmetric magnetic reconnection. Journal of Geophysical Research Space Physics, 2017, 122 (9), pp.9396-9413. 10.1002/2017JA024553 . hal-01895716

HAL Id: hal-01895716

https://hal.science/hal-01895716v1

Submitted on 2 Dec 2021

HAL is a multi-disciplinary open access archive for the deposit and dissemination of scientific research documents, whether they are published or not. The documents may come from teaching and research institutions in France or abroad, or from public or private research centers.

L'archive ouverte pluridisciplinaire **HAL**, est destinée au dépôt et à la diffusion de documents scientifiques de niveau recherche, publiés ou non, émanant des établissements d'enseignement et de recherche français ou étrangers, des laboratoires publics ou privés.

Copyright

AGU PUBLICATIONS

JGR

Journal of Geophysical Research: Space Physics

RESEARCH ARTICLE

10.1002/2017JA024553

Special Section:
Magnetospheric Multiscale (MMS) mission results throughout the first primary mission phase

Key Points:
- Observations of cold ion heating associated with magnetic reconnection
- Large electric field fluctuations (gradients and waves) in association with the cold ion heating
- At least 10 to 25% of the energy that goes into heating is used to heat cold ions

Supporting Information:
- Supporting Information S1
- Figure S1

Correspondence to:
S. Toledo-Redondo,
sergiotr@ugr.es

Citation:
Toledo-Redondo, S., et al. (2017), Energy budget and mechanisms of cold ion heating in asymmetric magnetic reconnection, *J. Geophys. Res. Space Physics*, *122*, 9396–9413, doi:10.1002/2017JA024553.

Received 1 JUL 2017
Accepted 20 AUG 2017
Accepted article online 28 AUG 2017
Published online 18 SEP 2017

©2017. American Geophysical Union. All Rights Reserved.

Energy budget and mechanisms of cold ion heating in asymmetric magnetic reconnection

Sergio Toledo-Redondo[1], Mats André[2], Yuri V. Khotyaintsev[2], Benoit Lavraud[3], Andris Vaivads[2], Daniel B. Graham[2], Wenya Li[2], Denise Perrone[1], Stephen Fuselier[4,5], Daniel J. Gershman[6], Nicolas Aunai[7], Jérémy Dargent[3,7], Barbara Giles[6], Olivier Le Contel[7], Per-Arne Lindqvist[8], Robert E. Ergun[9], Christopher T. Russell[10], and James L. Burch[4]

[1]European Space Agency, ESA/ESAC, Madrid, Spain, [2]Swedish Institute of Space Physics, Uppsala, Sweden, [3]Institut de Recherche en Astrophysique et Planétologie, CNRS, UPS, CNE, Université de Toulouse, Toulouse, France, [4]Southwest Research Institute, San Antonio, Texas, USA, [5]Department of Physics and Astronomy, University of Texas at San Antonio, San Antonio, Texas, USA, [6]NASA Goddard Space Flight Center, Greenbelt, Maryland, USA, [7]Laboratoire de Physique des Plasmas, UMR7648, CNRS, Ecole Polytechnique, UPMC Univ Paris 06, Univ. Paris-Sud, Observatoire de Paris, Paris, France, [8]Royal Institute of Technology, Stockholm, Sweden, [9]Laboratory of Atmospheric and Space Physics, University of Colorado Boulder, Boulder, Colorado, USA, [10]Earth Planetary and Space Sciences, University of California, Los Angeles, California, USA

Abstract Cold ions (few tens of eV) of ionospheric origin are commonly observed on the magnetospheric side of the Earth's dayside magnetopause. As a result, they can participate in magnetic reconnection, changing locally the reconnection rate and being accelerated and heated. We present four events where cold ion heating was observed by the Magnetospheric Multiscale mission, associated with the magnetospheric Hall **E** field region of magnetic reconnection. For two of the events the cold ion density was small compared to the magnetosheath density, and the cold ions were heated roughly to the same temperature as magnetosheath ions inside the exhaust. On the other hand, for the other two events the cold ion density was comparable to the magnetosheath density and the cold ion heating observed was significantly smaller. Magnetic reconnection converts magnetic energy into particle energy, and ion heating is known to dominate the energy partition. We find that at least 10–25% of the energy spent by reconnection into ion heating went into magnetospheric cold ion heating. The total energy budget for cold ions may be even higher when properly accounting for the heavier species, namely helium and oxygen. Large **E** field fluctuations are observed in this cold ion heating region, i.e., gradients and waves, that are likely the source of particle energization.

Plain Language Summary The magnetic field of Earth creates a natural shield that isolates and protects us from the particles and fields coming from our star, the Sun. This natural shield is called the magnetosphere and is filled by plasma. The particles coming from the Sun form another plasma called the solar wind and are usually deviated around the magnetosphere. However, under certain circumstances these two plasmas can reconnect (magnetic reconnection), and part of the energy and mass of the two plasmas is interchanged. Magnetic reconnection is the driver of storms and substorms inside the magnetosphere. In this work, we investigate what occurs to particles of very low energy (cold ions) of ionospheric origin when they reach the reconnecting boundary of the magnetosphere. It is found that they are energized and take an important part of the energy spent in reconnecting the plasmas. The plasma boundary develops spatial structures and emits waves that are able to heat the cold ions. Once heated, these cold ions irreversibly will escape the Earth's magnetosphere to never come back to Earth.

1. Introduction

Magnetic reconnection is a fundamental plasma process that changes the magnetic field topology and releases energy stored in the fields. This process transfers the energy stored in the fields into the particles [e.g., *Priest and Forbes*, 2000; *Biskamp*, 2005]. Notably, reconnection is known to occur between the shocked solar wind, namely the magnetosheath, and the Earth's magnetosphere, being the major driver of energy and

particle entry into the magnetospheric system. The coupling between these two plasma regimes depends to a large extent on the solar wind upstream conditions like the magnetic field orientation, the density, or the plasma pressure.

Magnetic reconnection occurring at the dayside magnetosphere is known to be asymmetric owing to the different nature of the two plasmas involved, i.e., the shocked solar wind (magnetosheath) and the magnetosphere [e.g., *Sonnerup*, 1974; *Haerendel et al.*, 1978; *Swisdak and Drake*, 2007; *Cassak and Shay*, 2007; *Pritchett*, 2008]. The magnetosheath is often composed of ions (mainly protons and a few percent of alpha particles) with temperatures ranging from few hundred eV up to few keV and electrons with temperatures of several tens to few hundred eV. The dayside magnetosphere is populated with a mixture of hot (up to tens of keV) and cold (up to few tens of eV) ion populations [e.g., *Olsen*, 1982; *Sauvaud et al.*, 2001]. The first corresponds mainly to the ring current and its parameters are quite stable in terms of density and temperature, and it is accompanied by an electron population with temperatures up to few keV. On the other hand, the cold ion component is much more variable, with densities ranging from less than 1 cm^{-3} to several tens of cm^{-3}. The temperatures range from few eV to few tens of eV, and their presence is more common on the duskside than on the dawnside [*Chen and Moore*, 2006; *André and Cully*, 2012]. A cold electron component (up to few tens of eV) is observed in association with the cold ions. The variability of the cold plasma component depends on the global energy state of the magnetosphere and its ability to detach the cold component from the plasmasphere or directly from the ionosphere via the polar caps [*Darrouzet et al.*, 2008; *Borovsky and Denton*, 2006; *Lee et al.*, 2016].

The cold plasma component, when present, has several effects on the coupling between the magnetosheath and the magnetosphere. First, it mass loads the magnetospheric side, corresponding to a reduction in the Alfvén velocity and the reconnection rate in the region where the mass loading occurs [*Borovsky and Denton*, 2006; *Walsh et al.*, 2013; *Borovsky et al.*, 2013; *Walsh et al.*, 2014]. This leads to different local reconnection rates along the X line. In addition, cold ions have a much smaller gyroradius (~10 km) than the magnetosheath (~250 km) and hot magnetospheric (~300 km) ions. Therefore, they introduce a new length scale into reconnection that leads to multiple effects, like, for instance, changes in the balance of the Hall **E** field [*Toledo-Redondo et al.*, 2015; *André et al.*, 2016], modified ion diffusion regions [*Toledo-Redondo et al.*, 2016a; *Divin et al.*, 2016], or an extended Larmor **E** field region [*Dargent et al.*, 2017].

Reconnection has the ability of transferring energy from the fields into the particles, creating exhausts (jets) embedded within the current sheet that sustains magnetic reconnection. Understanding both the amount of energy converted from fields to particles and the mechanisms involved in the conversion is one of the key problems of magnetic reconnection. *Aunai et al.* [2011] showed from simulations that the energy transferred by reconnection into the particles goes mainly in the form of heating rather than bulk acceleration. *Eastwood et al.* [2013] showed using observations from the Cluster spacecraft [*Escoubet et al.*, 2001] in the Earth's magnetotail that most of the energy in the outflow region was in the form of ion heating. *Phan et al.* [2014] performed a statistical analysis of ion bulk acceleration and heating using Time History of Events and Macroscale Interactions during Substorms spacecraft [*Angelopoulos*, 2009] observations. They found that roughly 20% of the available magnetic energy went into ion heating ($T_{i||} \simeq 2T_{i\perp}$) and that the ion heating was 8 times larger than the electron heating, although the simulations by *Haggerty et al.* [2015] suggested that the ion to electron heating ratio may depend on the upstream electron temperature. *Hietala et al.* [2015] studied the ion heating by reconnection in the magnetotail both using simulations and observations of the Cluster spacecraft. They found that $T_{i||}$ dominates at the boundaries, driving the firehose instability, while $T_{i\perp} > T_{i||}$ at the center of the exhaust, associated to Speiser-like meandering orbits.

All the mentioned studies did not discuss in detail the magnetospheric cold ion component. More recently, *Toledo-Redondo et al.* [2016b] showed evidence of magnetospheric cold ion heating in the magnetospheric separatrix region, upstream of the exhaust core, using Cluster spacecraft measurements. The heating reported was perpendicular to the magnetic field and occurred in association with large Hall **E** fields and waves. They pointed at mechanisms different from the pickup process, which occurs farther downstream inside the exhaust [*Wu et al.*, 1998; *Drake et al.*, 2009]. *Toledo-Redondo et al.* [2016b] discussed two mechanisms for ion heating that were consistent with the observations: waves at the ion cyclotron frequency [*André et al.*, 1994] and large electric field gradients [*Cole*, 1976; *Lindstedt et al.*, 2010], in association with the Hall electric field.

Left-hand polarized (LHP) waves oscillating at the ion cyclotron frequency can transfer energy from the fields to the particles via resonant acceleration [*Chang et al.*, 1986; *André et al.*, 1994]. The **E** field of the wave follows

the gyromotion of the particles transferring perpendicular momentum to them. The ion cyclotron heating rate is given by

$$\frac{dW}{dt} = P_i \frac{q^2}{2m} \tag{1}$$

where q and m are the charge and mass of the ions and P_i is the spectral density of the perpendicular electric field ($E_\perp$ at the ion gyrofrequency due to (incoherent) LHP waves) [*Chang et al.*, 1986]. Here the plasma is assumed to be homogenous and the wavelengths to be large compared to the ion gyroradius, so spatial effects are not important.

When the plasma is not homogeneous, large gradients of the **E** field can break the gyromotion and transfer energy to the particles [*Cole*, 1976; *Stasiewicz et al.*, 2000]. To irreversibly transfer energy to the ions, rather than causing **E**×**B** drift, $E_\perp$ should change significantly over an ion gyroradius. Considering a single test particle, for an electric field gradient parallel to **E** the energization condition is

$$/\nabla \mathbf{E}/ > qB^2/m \tag{2}$$

where q is the charge of the particle, B is the magnetic field amplitude, and m is the mass of the particle. *Stasiewicz et al.* [2013] suggested that this mechanism can be responsible of energization of ions in the foreshock region up to 1 MeV. Recently, *Catapano et al.* [2016] studied how the fluctuations in the magnetic field can energize the different ion species using test particle simulations.

The cold ion heating in the separatrix region reported by *Toledo-Redondo et al.* [2016b] is not always present; they showed an example where the cold ion component remained cold inside an exhaust region. The observed electric field fluctuations in space and time were not large enough to energize the ions for that event. They suggested that this situation could be common far away from the X line, where less free energy is present. More recently, *Graham et al.* [2017] reported lower hybrid drift wave observations in the vicinity of the ion diffusion region and also observed cold ion heating, and suggested the lower hybrid waves as a possible mechanism for cold ion heating.

In this work, we use high-resolution measurements made by the Magnetospheric Multiscale mission (MMS) [*Burch et al.*, 2015] to study cold ion heating associated with magnetic reconnection. These measurements allow us to quantify the amount of heating with better accuracy and to study the spatial variations in the heating region by taking advantage of the tetrahedron constellation. In section 2 we present a summary of the observations of four different events where cold ion heating was present. In section 3 we summarize the observations, discuss the impact over the global energy budget, and have a closer look to the mechanisms responsible for the cold ion heating. Finally, in section 4, we summarize the main conclusions of this study.

2. Results

In this section we show four events that contain observations of cold ion heating in association with magnetic reconnection at the Earth's dayside magnetopause. The MMS fleet made these observations during October 2015. MMS is composed of four identical spacecraft and have an equatorial orbit optimized to form a tetrahedron during the magnetopause encounters. In October 2015 the magnetopause crossings occurred at the duskside, where cold ions are commonly observed [*Chen and Moore*, 2006; *André and Cully*, 2012; *Fuselier et al.*, 2016]. The spacecraft separation for the events described below varied between 15 and 30 km. We use measurements taken by the following instruments on board MMS: the fluxgate magnetometer [*Russell et al.*, 2014] for low-frequency and background magnetic field measurements, the Search Coil Magnetometer (SCM) [*Le Contel et al.*, 2016] for high-frequency magnetic field measurements, the Spin-plane Double Probes [*Lindqvist et al.*, 2014] and the Axial Double Probes [*Ergun et al.*, 2016] for 3-D electric field measurements, the Fast Plasma Investigation (FPI) [*Pollock et al.*, 2016] for high-resolution measurements of the ions (150 ms) and electrons (30 ms), and finally the Hot Plasma Composition Analyzer (HPCA) [*Young et al.*, 2016] for mass resolved ion measurements.

2.1. Event 1

Figure 1 shows an MMS magnetopause crossing from the magnetosphere into the Magnetosheath Boundary Layer (MSBL), hereinafter referred as to event 1, in *LMN* coordinates. It occurred on 9 October 2015, at [8.7, 7.5, −0.3] Earth radii in GSE coordinates, with the spacecraft in tetrahedron formation at distances of ∼30 km.

The data shown corresponds to MMS1 except for the products that use multispacecraft techniques (motion of the boundary and gradients of the electric field). The **N** = [0.89, 0.11, −0.45]) component is obtained using Minimum Variance Analysis applied to the magnetic field. **L** = [0.41, 0.23, 0.86] is chosen to be perpendicular to **N** and close to the magnetospheric **B** field (i.e., roughly **Z** GSE), and **M** = [0.20, −0.95, 0.16] closes the system. The magnetic field is shown in Figure 1a, where the magnetopause crossing is observed as a rotation in the **L** component. There is a strong B_M component that we identify as a bipolar Hall signature [*Pritchett and Mozer*, 2009]. Its large value suggests proximity to the X line. Figure 1b shows $\mathbf{E} + \mathbf{v}_i \times \mathbf{B}$. The peak of the Hall electric field in the ion frame, $(E + v_i \times B)_N = 9$ mV/m, is observed at 09:37:39 UT. This electric field can be supported by pressure gradient, inertial, and anomalous heating. The width of the Hall electric field region is estimated to be on the order of several hundred kilometers: MMS1 was inside this region roughly 5 s, and the normal component of the boundary velocity $v_{MP,n}$ during that interval changed between 100 and 200 km/s. We inferred the boundary velocity by cross-correlating **B** field measurements on the four spacecraft every 1 s, as described below. Therefore, the size of the Hall **E** field region was larger than the cold ion gyroradius ($\rho_c \approx$ 20 km for 15 eV ions, $\rho_c \approx 100$ km for 400 eV ions).

The total ion density (n_i) observed by FPI is plotted in black and the cold ion density (n_{ic}) in blue (Figure 1c). The blue line considers all ions below 1 keV. We also computed n_{ic} (blue crosses in Figure 1c) by selecting the relevant portion of the FPI sky map for each energy bin, allowing to separate cold ions and magnetosheath ions with better accuracy. This technique has been used previously by *André et al.* [2016] and *Toledo-Redondo et al.* [2016a]. This technique is also used to calculate the cold ion velocity (Figure 1e) and temperature (T_{ic}) (Figure 1h). More details on the cold ion moment calculation are given in the supporting information. The two methods are in good agreement for the density estimation. On the magnetospheric side the total density is roughly 1–2 cm^{-3} (mostly cold ions), it goes up to 3–4 cm^{-3} in the exhaust region and 7–8 cm^{-3} in the magnetosheath. After about 09:37:38 UT cold ions could not be identified as a separate population. Figure 1d shows the ion bulk velocity. The −**M** component of the magnetosheath plasma is consistent with the solar wind draping around the magnetosphere at the location of the spacecraft (duskside). The reconnection exhaust can be inferred from the v_L component (up to 400 km/s). We plot the cold magnetospheric ion velocity (v_{ic}) in the frame of the moving magnetopause boundary in Figure 1e. We obtained the boundary velocity vector v_{MP} by timing the magnetic field measurements at four spacecraft. We find the time difference between spacecraft by minimizing the cross correlation of the three **B** components for each pair of spacecraft. We applied this technique at 1 s intervals, finding the average magnetopause velocity vector every 1 s. The two methods described above for partial moment calculations (i.e., separate the cold ion component) have been used to obtain v_{ic} (solid lines correspond to all ions below 1 keV, and crosses correspond to portions of the sky map as detailed in the supporting information). From 09:37:37 UT onward, the two methods for v_{ic} calculation start to differ because exhaust ions below 1 keV are present. Between 09:37:32 UT and 09:37:36 UT we observe a cold ion velocity in the **N** direction of 40–50 km/s that we identify as the inflow velocity of magnetic reconnection. The omnidirectional ion Differential Energy Flux (DEF) is plotted in Figure 1f. The black line corresponds to the $\mathbf{E} \times \mathbf{B}$ energy, and the blue line marks the 1 keV total energy threshold used for cold ion moments calculation. The vertical black lines indicate the times when detailed cold ion moments were obtained. On the magnetospheric side (before 09:37:36 UT), both hot (with total energies of several keV to several tens of keV) and cold (with total energies up to few hundred eV) ions can be identified. First magnetosheath ions are detected at ∼09:37:36 UT (ion edge), and cold ions experience a temperature increase (Figure 1h), seen as a energy spread in the spectrogram (Figure 1f). Figure 1g shows the pitch angle distributions of ions below 1 keV in the spacecraft frame. Before MMS crosses the ion edge the cold ion population has a low temperature and most of their energy is due to their $\mathbf{E} \times \mathbf{B}$ motion. After crossing the ion edge, cold ions have larger temperature and exhibit broader pitch angles, and a portion of them moves parallel to **B**.

The cold ion temperature in field-aligned coordinates (FACs) is calculated for individual ion distributions by manually selecting the relevant bins, as commented above, and plotted in Figure 1h. The cold ion temperature is roughly 15 eV at the beginning of the interval (inflowing magnetosphere), and reaches ∼400 eV at 09:37:37.7 UT. This temperature increase is anisotropic and mainly in the perpendicular direction, although there is a nonnegligible parallel temperature increase of the cold ions. The total ion temperature is plotted in green. Inside the exhaust region, the cold ion temperature is roughly equal to the total temperature ($T_{\mathrm{ci}} \simeq T_i$). Large gradients of the electric field (see equation (2) can alter the gyromotion of magnetized particles. The change in motion depends on the angle of arrival of the particle and determines the amount of energy transferred to the ion [*Cole*, 1976; *Stasiewicz et al.*, 2000; *Lindstedt et al.*, 2010]. The electric field gradient is

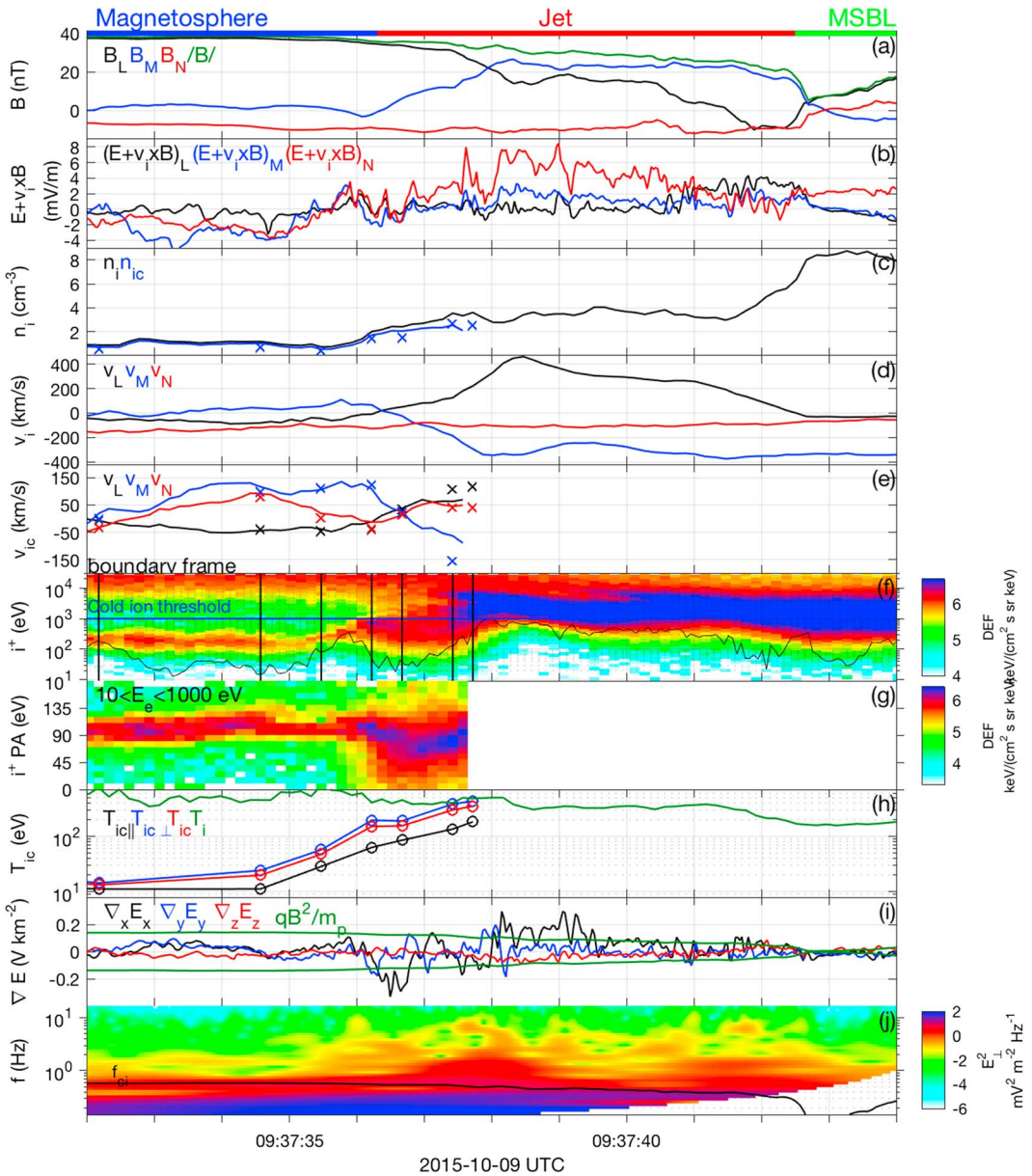

Figure 1. MMS1 observations of event 1 (9 October 2015) in *LMN* coordinates. (a) Magnetic field. (b) Electric field in the plasma frame (**E**+$\mathbf{v}_i$×**B**). (c) Ion density: total (black) and cold ion density (blue). (d) Ion bulk velocity. (e) Cold ion velocity in the magnetopause frame. Lines correspond to all ions below 1 keV, and crosses correspond to the method described in the supporting information for cold ion moment calculation. (f) Ion differential energy flux (DEF). The horizontal blue line marks the 1 keV threshold for cold ion moment calculation. Black vertical lines indicate the times when detailed cold ion moment calculation was obtained (see supporting information). (g) Pitch angle of ions with total energy below 1 keV. (h) Total ion temperature (green) and cold ion temperature in FAC coordinates (black, blue, and red). (i) Electric field gradient calculated using four spacecraft, compared to right-hand side of equation (2) (green). (j) Perpendicular **E** field power wavelet spectrogram. f_{ci} is plotted in black.

computed from four spacecraft measurements and plotted, together with the right-hand side of equation (2), in Figure 1i. The gradient of the electric field vector corresponds to a tensor, but we plot only the diagonal terms, which correspond to gradients in the direction of the electric field. Assuming errors of ~2 mV/m in the **E** field measurement and taking into account the spacecraft separation (30 km for this event), the uncertainty in ∇**E** is ~0.067 V/km^2. Figure 1i indicates that there are large gradients of the **E** field that fulfill the condition of equation (2) and therefore can account for at least part of the perpendicular heating observed. Figure 1j shows the wavelet spectrogram of the perpendicular components of the electric field. The ion cyclotron

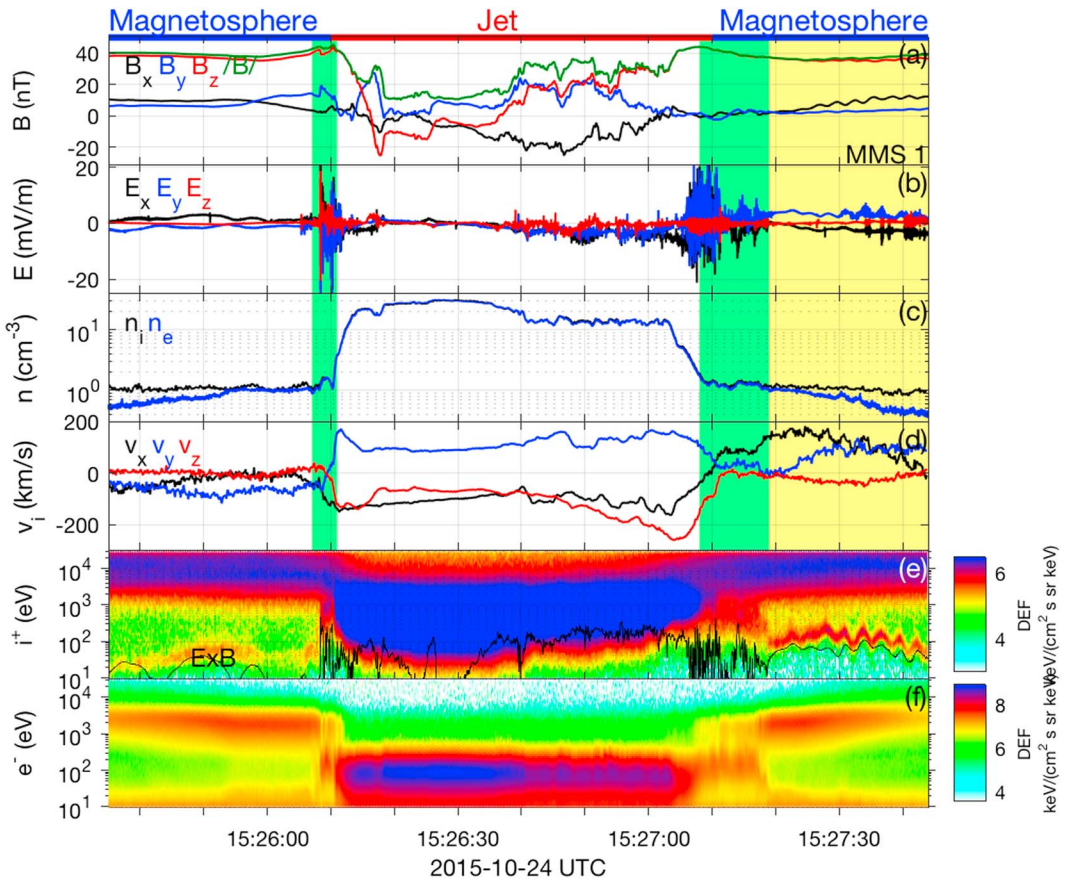

Figure 2. MMS1 overview of event 2 (24 October 2015) in GSE coordinates. (a) Magnetic field. (b) Electric field. (c) Ion (black) and electron (blue) densities. (d) Ion bulk velocity. (e) Ion differential energy flux. **E** × **B** energy is plotted in black. (f) Electron differential energy flux.

frequency is plotted using a black line. Assuming that the electric field variations correspond to time variations, an increase in the wave activity is observed in the cold ion heating region and the exhaust, starting around 09:37:35.5 UT. Time variations of the **E** field can energize particles if they are in resonance (see equation (1), as discussed in more detail in section 3.

2.2. Event 2

Another MMS magnetopause encounter is presented in Figure 2 (hereinafter referred as to event 2), which occurred on 24 October 2015, with a spacecraft separation of ∼15 km. The data shown for discussion of event 2 correspond to MMS1 unless otherwise stated. MMS was initially in the magnetosphere, crossed into a reconnection jet and back to the magnetosphere in 1 min approximately. The two crossings show different normal directions and flow velocities, suggesting that reconnection was time varying. Cold ions are present at the magnetopause, and they are heated in the vicinity of the boundary (green-shadowed regions in Figure 2). We observed large electric field fluctuations (Figure 2b) in the cold ion heating region. The density ratio between the magnetospheric side (∼1 cm^{-3}, mainly cold ions) and the exhaust region (20–30 cm^{-3}) is large. The ion bulk velocity observed by FPI is plotted in Figure 2d in GSE coordinates in spacecraft frame. The jet velocity is on average (−110, 115, −115) km/s. In the yellow-shadowed region, we observe velocity fluctuations in the **X** and **Y** components, consistent with fluctuations in **B** (Figure 2a) and **E** (Figure 2b). The period of these fluctuations is on the order of 3 s. We can distinguish the magnetosheath (tens of eV to several keV), hot magnetospheric (few keV to tens of keV), and cold magnetospheric (below 1 keV) populations in the omnidirectional ion DEF (Figure 2e). In the green-shadowed regions the cold ions are heated. In the yellow-shadowed region cold ions are accelerated but not heated, as discussed later. The omnidirectional electron DEF is shown in Figure 2f. In the green-shadowed regions, we observe an electron population with energies between several tens of eV and few hundred eV. It corresponds to cold electrons that have been heated. Although they have

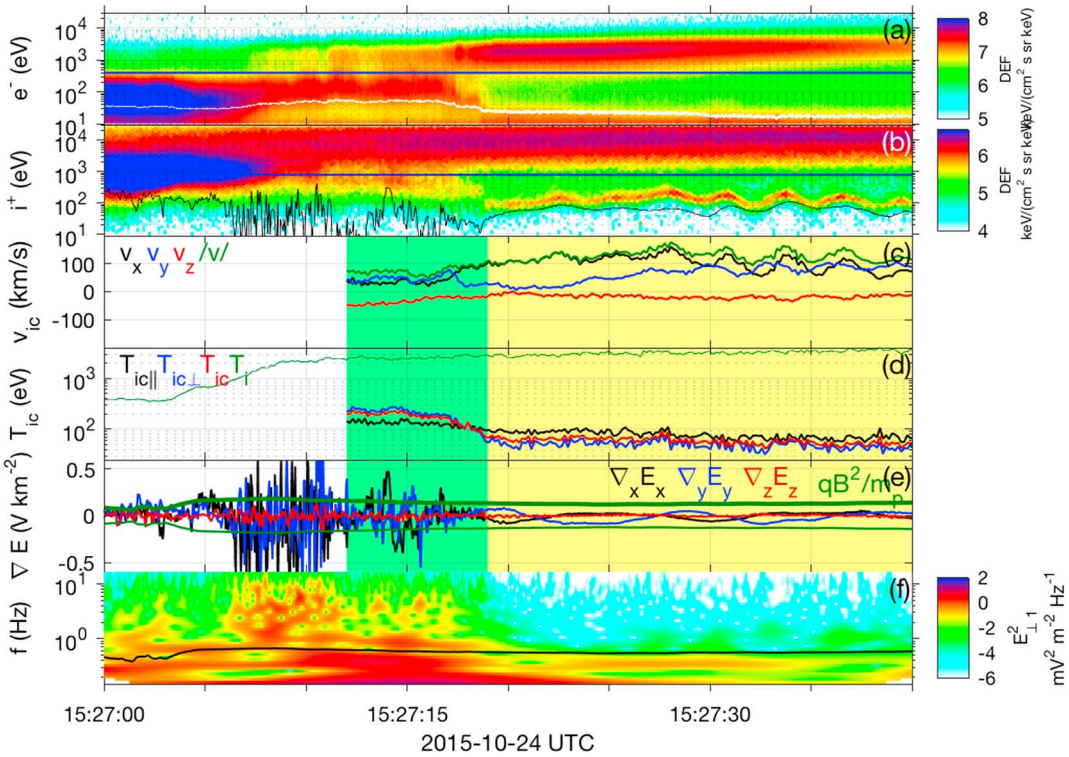

Figure 3. Detail of MMS1 observations of second crossing of event 2. (a) Omnidirectional electron differential energy flux. Electron temperature below 400 eV (blue line) is plotted in white. (b) Omnidirectional ion differential energy flux. Blue line (800 eV) represents the threshold for cold ion moment calculation. Black line corresponds to $\mathbf{E} \times \mathbf{B}$ energy. (c) Cold ion velocity. (d) Cold ion (T_{ic}) in FAC coordinates (black, blue, and red) and total ion (T_i, green) temperatures. (e) Electric field gradient calculated using four spacecraft, compared to the right-hand side of equation (2). (f) Perpendicular **E** field power wavelet spectrogram. f_{ci} is plotted in black.

similar energies to those coming from the magnetosheath, their density is much lower and consistent with magnetospheric density, indicating that they correspond to a cold electron component of magnetospheric origin. On the magnetospheric side (for example, in the yellow-shadowed region), these cold electrons have energies below 10 eV and FPI cannot detect them. This results in an underestimation of the total electron density in that region (Figure 2c).

Next, we take a closer look to the second crossing (15:27:00 UT–15:27:40 UT). Figure 3a shows the electron spectrogram, where cold and hot magnetospheric electrons are seen in the yellow-shaded region. The cold electron temperature (T_{ec}) for electrons of energies below 400 eV is plotted in white. The cold electrons do not correspond to photoelectrons since the spacecraft potential is below 10 eV, the lower energy threshold of the measurement. The cold electrons have been heated from less than ~15 eV in the magnetosphere to ~50 eV inside the green-shadowed region (see T_{ec}, white curve), and their temperature is larger than for magnetosheath electrons (~35 eV), which are observed before ~15:27:08 UT. In the region where cold electrons are heated, the same occurs for cold ions (Figure 3b). In the yellow-shaded region cold ions have total energies close to the $\mathbf{E} \times \mathbf{B}$ energy (black line) and are accelerated and decelerated together consistent with the **E** and **B** wave motion. The frequency of the wave (~0.33 Hz) is below the ion cyclotron frequency (see Figure 3f), and no cyclotron heating occurs. We computed partial moments (velocity in Figure 3c and temperature in Figure 3d) of the ions below the blue line (800 eV) of Figure 3b (cold ions). We can see cold ion velocity fluctuations consistent with **B** and **E** fluctuations (see Figure 2). In contrast, the cold ion temperature (Figure 3d) remains constant over the low-frequency wave region (yellow-shadowed region), indicating that no ion heating occurs. In the green-shadowed region, the cold ions are heated perpendicularly ($T_{ic\perp}$ ~300 eV, blue), while the parallel temperature (black) does not exceed 150 eV. The total ion temperature (T_i, green curve) in the exhaust region is larger (~400 eV) than the cold ion temperature observed. We computed $\nabla\mathbf{E}$ using the measurements of four spacecraft (15 km separation) and compared them to qB^2/m_p in Figure 3e, (uncertainty in $\nabla\mathbf{E}$ is ~0.13 V/km^2 assuming errors of ~2 mV/m in the electric field). For the yellow-shaded region the

condition for heating is not satisfied (see equation (2), consistent with the observations. On the other hand, the $\nabla\mathbf{E}$ becomes large in the heating region and exceeds the value of qB^2/m_p and may contribute to the perpendicular cold ion heating observed. In addition, the power spectral density of the perpendicular electric field (Figure 3f) becomes larger inside the heating and the exhaust regions, both at f_{ci} and larger frequencies, and can be also responsible for part of the ion heating observed.

2.3. Event 3

In Figure 4 we show another magnetopause encounter by MMS on 10 October 2015 (hereinafter referred as to event 3), with ~30 km spacecraft separation. The data shown for discussion of event 3 correspond to MMS4 unless otherwise stated, because the heavy ion signatures on FPI (see below) are clearer than for the other spacecraft. MMS4 moved from the magnetosphere into a reconnection jet and back into the magnetosphere in ~12 s. The two crossings show different bulk flows and magnetic field rotations indicating transient effects on the jet. The densities on the magnetospheric side and inside the jet were similar (~4 cm^{-3}, Figure 4c) owing to the cold ions of the magnetospheric side, which increase the density of the magnetosphere. The ion jet velocity is on average (−210, 175, −175) km/s in GSE coordinates in spacecraft frame. Clear signatures of $\mathbf{E}\times\mathbf{B}$ drifting cold H^+ and He^+ can be observed in the magnetospheric side (Figures 4e and 4f), close to the first and second crossings. Signatures of O^+ seem also to be present between 07:14:40 UT and 04:14:48 UT although these are fainter. HPCA also detected He^+ (Figure 4h) in addition to H^+ (Figure 4g) that match to the $\mathbf{E}\times\mathbf{B}$ energy, indicating that they belong to the cold plasma component (plume). We computed the electric field gradients observed by MMS using four spacecraft measurements (Figure 4i) and compared them to the right-hand side of equation (2) (qB^2/m), for H^+ (green) and He^+ (gray). The spacecraft separation is 30 km, and the error associated to $\nabla\mathbf{E}$ is ~0.067 V/km^2. The $\nabla\mathbf{E}$ fields are large enough to produce heating at the boundary between the magnetosphere and the jet and inside jet, i.e, satisfy the condition stated in equation (2). This condition is easier to satisfy for He^+ than for H^+. Finally, the perpendicular $\mathbf{E}$ field power spectrum (Figure 4j) also shows an increase at f_{ci} and higher frequencies in the region where the jet is observed.

Next, we look at the individual ion sky maps to separate H^+ and He^+ (see supporting information) and compute their partial moments. Density (Figure 5a), velocity (Figure 5b), and temperature (Figure 5c) are obtained separately for both H^+ and He^+ using FPI measurements (150 ms). This has potential issues because FPI was not designed and calibrated for different species than protons, but our consistency checks, namely comparisons with HPCA He^+ density and $\mathbf{E}\times\mathbf{B}$ velocity, show that the He^+ high-resolution moments obtained using FPI are reliable. The total ion density is 2–4 cm^{-3} (black, FPI) and corresponds mainly to cold protons (blue, FPI), while the He^+ density is 0.24 cm^{-3} (red and gray, FPI and HPCA, respectively). We note the good agreement between FPI and HPCA after corrections are made to account for the mass difference between the two species. On the magnetospheric side (i.e., after 07:14:40.5 UT), the velocity of the two cold plasma species (Figure 5b) is similar and roughly consistent to $\mathbf{E}\times\mathbf{B}$ drift motion plus a parallel component in the $-\mathbf{Z}$ direction. The He^+ velocity is in good agreement with H^+ and the $\mathbf{E}\times\mathbf{B}$ velocity outside the heating region (white-shadowed), indicating that the FPI calculation of the He^+ velocity moment was robust. We separate the observations into three regions based on the temperature of the H^+ and He^+. In the first region (magnetospheric side, i.e., after 07:14:40.5 UT), both H^+ and He^+ have temperatures similar or below 10 eV. These temperatures are comparable to the energy resolution of FPI, and the uncertainty of the cold ion temperature is of the order of the measurement. In the green-shadowed region, He^+ is heated up to ~100 eV while the proton temperature remains similar to 10 eV. The spatial size of this region is roughly 150 km, based on the normal component of the boundary velocity ($v_{MP,n}$ ~150 km/s) obtained from correlations of four spacecraft $\mathbf{B}$ field measurements. This corresponds to a few He^+ gyroradii, so finite gyroradius effects can be present (the gyroradius of He^+ for /B/=40 nT and T_{He^+}=50 eV is ~50 km). We interpret that the heating region for He^+ is larger than for H^+ owing to their larger gyroradius. Finally, closer to the jet, the cold protons also experience heating up to ~70 eV. Inside this region we could not trace the He^+ anymore to compute their temperature. We expect them to be hotter, and this may be the reason why we cannot observe them (the $\mathbf{E}\times\mathbf{B}$ energy goes down, the cold ions are heated, and they split over several energy channels, ending up with too low counts at each energy channel). The total ion temperature (T_i ~1 keV, red) is much larger owing to the presence of the hot magnetospheric population. In the omnidirectional (Figure 5d) and perpendicular (Figure 5e) ion DEF spectrograms we can observe the drifting cold H^+, He^+, and probably O^+ populations. The electric field fluctuations become larger inside the region where the cold ion heating is observed (Figure 5f). We have a closer look to $\nabla\mathbf{E}$, compared to qB^2/m, in Figure 5g. We can see that for this time interval the condition of equation (2) is satisfied for He^+

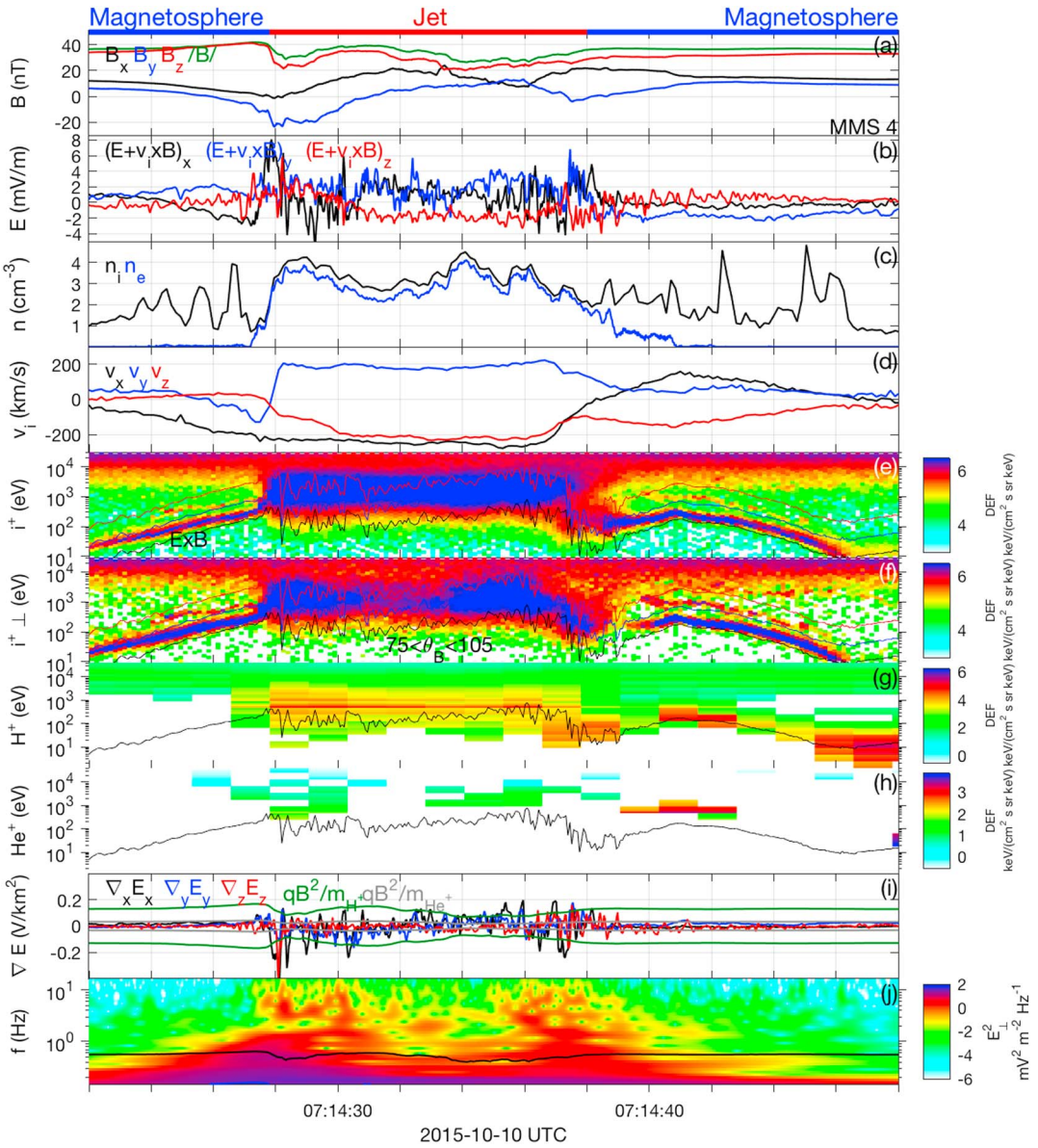

Figure 4. MMS4 observations of event 3 (10 October 2015) in GSE coordinates. (a) Magnetic field. (b) Electric field in the plasma frame (**E**+$\mathbf{v}_i\times$**B**). (c) Ion (black) and electron (blue) densities. (d) Ion bulk velocity. (e) Omnidirectional ion differential energy flux. Black, blue, and red lines correspond to **E** $\times$ **B** energy for protons, He+, and O+, respectively. (f) Perpendicular ion differential energy flux. Black, blue, and red lines correspond to **E** $\times$ **B** energy for protons, He^+, and O^+, respectively. (g) HPCA ion energy flux for protons (subspin resolution). (h) HPCA ion energy flux for He^+ (subspin resolution). (i) Electric field gradient calculated using four spacecraft. (j) Perpendicular **E** field power wavelet spectrogram. f_{ci} is plotted in black.

(gray), but it is only marginally satisfied for H^+ (green). The perpendicular **E** field wavelet spectrogram indicates an increase in the wave activity in the yellow-shadowed region (proton heating region), see Figure 5h.

2.4. Event 4

Another interesting magnetopause encounter with the presence of cold ions, hereinafter referred as to event 4, occurred the 24 October 2015 at 05:04 UTC (~10 h before than event 2, during the outbound of the same orbit). It is summarized in Figure 6 using MMS1 observations, where three different regions have been marked: the magnetosphere, the exhaust, and the MSBL regions. The magnetopause crossing is observed as a magnetic field reversal in **Z** (Figure 6a). The cold ion moments for event 4 were calculated in two ways: all ions below 400 eV (solid lines in Figure 6b for density and Figure 6d for velocity) and as detailed in the

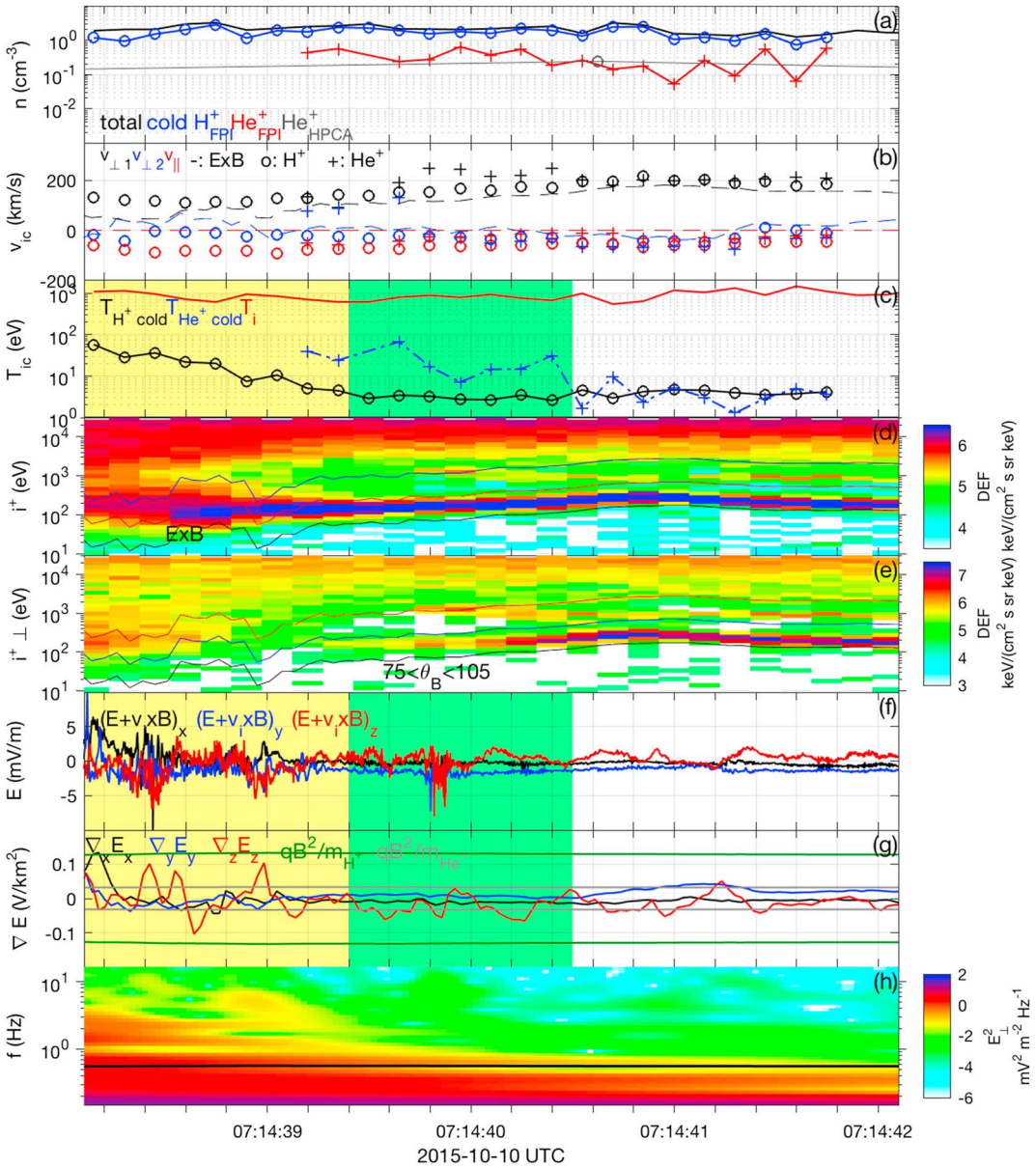

Figure 5. Detail of MMS4 observations of the second crossing of event 3. (a) Total ion density (black), cold H^+ density from FPI (blue), cold He^+ density from FPI (red), and He^+ density from HPCA (gray). (b) Velocity of cold H^+ (circles), velocity of cold He^+ (crosses), and $\mathbf{E} \times \mathbf{B}$ velocity (solid). (c) Cold ion temperature for protons (black) and He^+ (blue). The total ion temperature is plotted in red. (d) Omnidirectional ion differential energy flux. Black, blue, and red lines correspond to $\mathbf{E} \times \mathbf{B}$ energy for protons, He^+ and O^+, respectively. (e) Perpendicular ion differential energy flux. Black, blue, and red lines correspond to $\mathbf{E} \times \mathbf{B}$ energy for protons, He^+ and O^+, respectively. (f) Electric field in the plasma frame ($\mathbf{E} + \mathbf{v}_i \times \mathbf{B}$) in GSE coordinates. (g) Electric field gradient from combining four spacecraft measurements. The right-hand side of equation (2) (qB^2/m) is plotted for protons (green) and He^+ (gray). (h) Perpendicular $\mathbf{E}$ field power wavelet spectrogram. f_{ci} is plotted in black.

supporting information (circles in Figures 6b, 6d, and 6i are for temperature). The cold ion density (n_{ic}) is variable along the crossing, on the order of 5–10 cm^{-3}, being the dominant population in the magnetosphere and inside the exhaust (Figure 6b). On the magnetosheath side, the density is ~10–15 cm^{-3}. In Figure 6c the total ion bulk velocity is plotted. It is consistent with $\mathbf{E}\times\mathbf{B}$ drift plus an antiparallel motion roughly in the $-\mathbf{Z}$ direction, i.e, a southward jet, which defines the jet region (05:03:52 UT–05:04:15 UT), peaking at −200 km/s. The cold ion velocity (Figure 6d, solid lines) shows that the cold ions do not follow the antiparallel $-\mathbf{Z}$ motion of the exhaust ions and correspond purely to the $\mathbf{E} \times \mathbf{B}$ drift (dashed lines). Next, we show ion differential

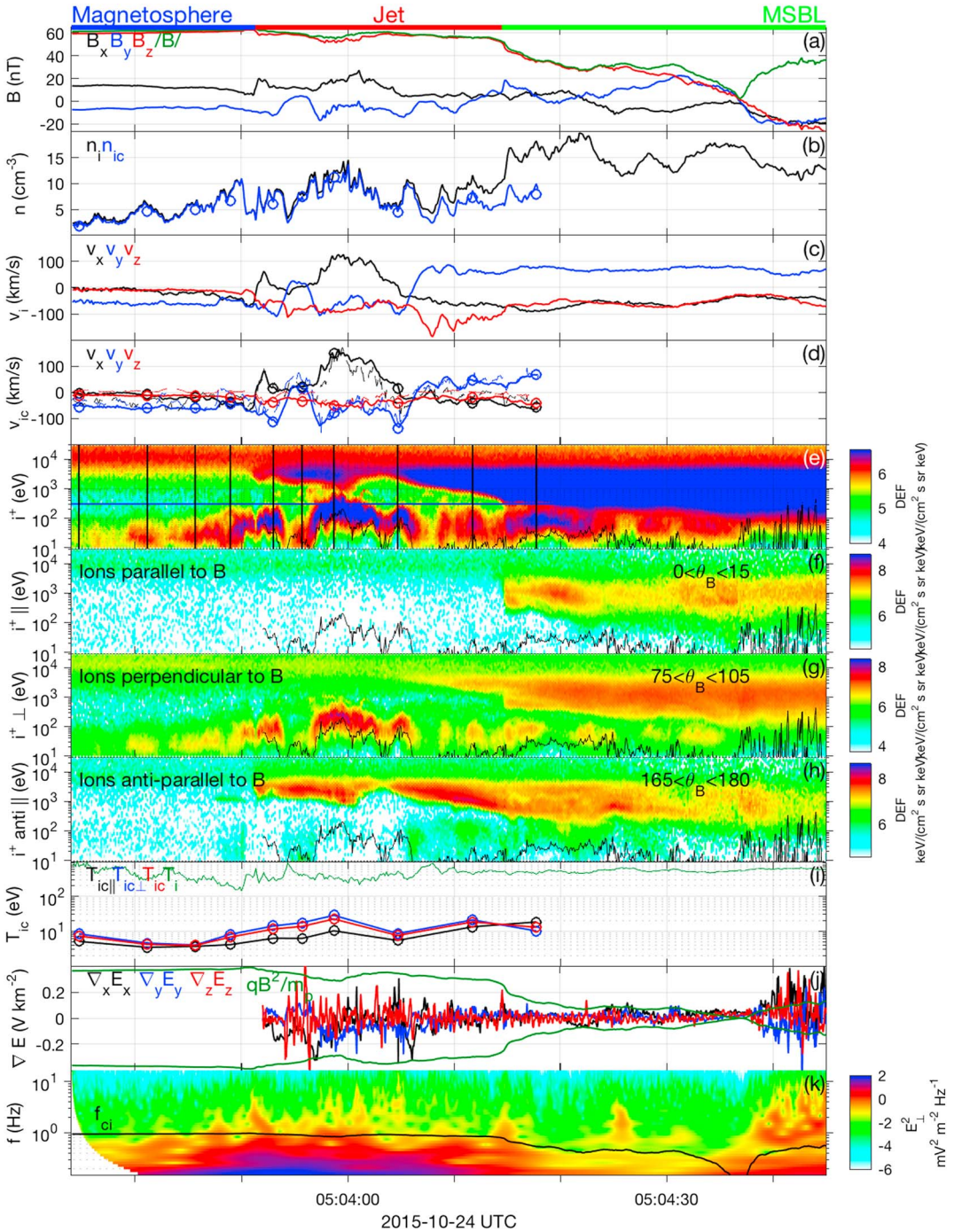

Figure 6. MMS1 observations of event 4 in GSE coordinates. (a) Magnetic field. (b) Total (black) and cold (blue) ion densities. (c) Ion bulk velocity in GSE coordinates. (d) Cold ion velocity in GSE coordinates (solid lines and circles) and **E** × **B** velocity (dashed lines). (e) Omnidirectional ion differential energy flux. Vertical lines indicate the distributions where accurate cold ion temperature was manually calculated. (f) Parallel ion differential energy flux. (g) Perpendicular ion differential energy flux. (h) Antiparallel ion differential energy flux. (i) Cold ion temperature in FAC coordinates (black, blue, and red) and total ion temperature (T_i, green). (j) ∇**E** calculated using four spacecraft, compared to the right-hand side of equation (2) (green). (k) Perpendicular **E** field power wavelet spectrogram. f_{ci} is plotted in black.

energy flux spectrograms: omnidirectional, parallel to **B**, perpendicular to **B**, and antiparallel to **B** (Figures 6e–6h, respectively). Three ion populations can be distinguished based on their mean energy. Magnetospheric hot ions have energies around 10 keV and are mostly isotropic. Cold magnetospheric ions are observed around 100 eV (up to several hundred eV at 05:04:00 UTC), and their energy is mainly perpendicular to **B**. The cold ions follow $\mathbf{E} \times \mathbf{B}$ (Figure 6d) but do not follow the antiparallel direction of the exhaust population. The magnetosheath ions have energies roughly between the hot and the cold magnetospheric populations (from several hundred eV up to several keV). Inside the jet, the magnetosheath ions are mainly antiparallel to **B** (Figure 6h). However, there is a sharp boundary at 05:04:14.7 UT (Figure 6f) associated with a current sheet (rotation of **B**, Figure 6a) and an increase in the density (Figure 6b). After crossing the boundary, magnetosheath ions are also seen in the parallel and perpendicular directions.

We calculated the cold ion temperature of several representative ion distributions (marked with vertical lines in Figure 6e). For each of the ion distributions we manually selected the relevant portion of the sky map for each energy level where cold ions were observed. We plot the resulting ion temperature in field-aligned coordinates in Figure 6i. The cold ion temperature is mainly anisotropic, and it is below 40 eV for the whole interval. On the other hand, the total temperature (T_i, green) is roughly 500 eV. Cold ions of magnetospheric origin are observed in the three different regions (magnetosphere, exhaust, and magnetosheath) with similar temperatures. In Figure 6j we show the diagonal terms of $\nabla\mathbf{E}$ and compare them to the right-hand side of equation (2) (qB^2/m). The error associated to $\nabla\mathbf{E}$ is 0.13 V/km^2 (15 km spacecraft separation). The condition for heating is not fulfilled until 05:04:38 UT, when MMS observes a magnetic null ($B < 3$ nT). This is consistent with the low temperatures of the cold ions shown in Figure 6i, indicating that this mechanism did not heat the cold ions during this event. Figure 6k shows the wavelet spectrogram of the perpendicular component of the electric field. The ion cyclotron frequency (f_{ci}) is plotted on top. The energy available at f_{ci} is smaller than for the other events, as discussed in section 3.

3. Discussion

In the previous section we showed observations of cold ion heating in the inflow region of magnetic reconnection, close and inside the separatrix region (events 1–3). By contrast, event 4 shows the signatures of an exhaust (reconnection) but no cold ion heating. The cold ion heating is associated to large spatial gradients and time fluctuations (waves) of the **E** field. In this section we first discuss the implications of this cold ion population for the energy budget of reconnection. Then we discuss on the energy transfer mechanisms that may play a role in heating the cold ions.

We summarize in Table 1, for the four events discussed, the ambient values of the magnetic field for the magnetosphere and magnetosheath (B_m, B_s), the total densities (n_m, n_s), the cold ion temperature in the magnetosphere ($T_{\mathrm{ic},m}$), the maximum cold ion temperature observed ($T_{\mathrm{ic,max}}$), the ion temperature inside the exhaust ($T_{i,\mathrm{jet}}$) and in the magnetosheath (T_{is}), the predicted Alfvén velocity for asymmetric reconnection [*Cassak and Shay*, 2007], the distance to Earth, and the position of the spacecraft in GSE coordinates (r_{GSE}). n_m corresponds to the sum of cold and hot magnetospheric plasma. However, the hot component represents less than 10% of the total density, and hereinafter we will use $n_m \approx n_{\mathrm{ic}}$. Events 1 and 2 are in contrast with 3 and 4 when looking at the global parameters described in Table 1. First, the magnetospheric density (dominated by the cold component) is 10% or less of the magnetosheath density for events 1 and 2, while for events 3 and 4 it is close to 50%. Events 1 and 2 occurred at distances farther from Earth (11.5 and 10.9 Earth radii) than events 3 and 4 (10.3 and 9.5 Earth radii), which correspond to a more compressed magnetosphere. More cold ions are expected at the magnetopause when the magnetosphere is compressed. Second, the cold ion heating observed for events 1 and 2 was roughly of the order of the magnetosheath ion temperature, while for events 3 and 4 cold ions were heated only to a fraction of it (80 eV, i.e., 10% of magnetosheath ion temperature for event 3) or not heated at all (40 eV for event 4).

The energy budget in the outflow region is dominated by the ion heating [*Aunai et al.*, 2011; *Eastwood et al.*, 2013]. When cold ions are heated, they must take part of this energy. Based on the measurements of Table 1, we estimate the amount of energy that reconnection spends in heating the cold ions relative to the energy spent into heating the denser magnetosheath ions. To do so, we compare the increase of cold ion temperature $\Delta T_{\mathrm{ic}} = T_{\mathrm{ic,max}} - T_{\mathrm{ic},m}$, i.e., the final temperature minus the initial temperature, to the increase of magnetosheath

Table 1. Global Parameters of the Events

Event	B_m^a (nT)	B_s^b (nT)	n_m^a (cm^{-3})	n_s^b (cm^{-3})	$T_{ic,m}^a$ (eV)	$T_{ic,max}^c$ (eV)	$T_{i,jet}$ (eV)	T_{is}^b (eV)	v_A (km/s)	$/r_{GSE}/$ (R_E)	r_{GSE} (R_E)
1	40	15–20	1–2	10–12	15	400	400	200	200	11.5	[8.7, 7.5, −0.3]
2	40	20–30	1–2	20–30	60	250	400	250	170	10.9	[7.3, 8, −0.3]
3	40	20	2–4	4–6	10	80	900	750	300	10.3	[8.7, 5.6, −0.2]
4	60	30–40	3–10	10–20	10	40	400	300	290	9.5	[9.4, 3, −0.3]

[a]Subscript *m* stands for magnetosphere.
[b]Subscript *s* stands for magnetosheath.
[c]Maximum cold ion temperature observed inside the heating region.

ion temperature $\Delta T_{is} = T_{i,jet} - T_{is}$, and scale it to their relative densities. The relative amount of energy spent by reconnection in heating the cold ions ρ_{ic}, neglecting the sparse hot magnetospheric population, is

$$\rho_{ic} = \frac{\Delta T_{ic} n_{ic}}{\Delta T_{ic} n_{ic} + \Delta T_{is} n_{is}} \tag{3}$$

where the subscript ic stands for cold magnetospheric ions and the subscript is stands for magnetosheath ions. We find that for events 1–3, the cold ions take at least 20%, 8%, and 27%, respectively, of the total energy that went into ion heating. For event 3 we could calculate for the cold He^+ contribution (7% cold He^+, 20% cold H^+), and the total cold ion contribution is larger. The values of ρ_{ic} obtained correspond to a significant portion of the energy budget. The estimated energy budgets correspond only a lower threshold of the total heating that may go into cold ions, because once the cold ions become mixed with the magnetosheath ions we cannot determine if they continue to be heated, e.g., by the pickup process. Our results, based on four events, seem to indicate that at least 10–25% of the heating energy goes into cold ions despite the fact that the cold ion to magnetosheath density ratio varied significantly between the events. When there are less cold ions, they gain higher temperatures (events 1 and 2) than when there are many cold ions (event 3). Based on *Borovsky and Denton* [2008], plumes transport 2×10^{26} ions/s toward the dayside magnetopause during active periods. If the cold ions were heated up to 100 eV (conservative value), then this would result in reconnection spending 3.2 MW in cold ion heating during the time of the plume (up to few days).

The pickup process has been suggested to be one of the main mechanisms for energy conversion by reconnection in the exhausts. This mechanism accelerates the ions inside the exhaust owing to $\mathbf{E} \times \mathbf{B}$ force, and during this process ion heating may be produced as well [*Wu et al.*, 1998; *Drake et al.*, 2009]. It is not possible to distinguish cold magnetospheric ions from magnetosheath ions inside the exhausts of events 1–3. For these events, the $\mathbf{E} \times \mathbf{B}$ energy corresponds to the lower threshold of the exhaust population (black line in Figures 1f, 2e, and 4e) suggesting that magnetospheric cold ions could have been accelerated and heated by the pickup process. By contrast, in event 4 the $\mathbf{E} \times \mathbf{B}$ energy (few to several tens of eV) is much lower than the lower threshold of the exhaust population (several hundred eV), see Figure 6e. The exhaust ion velocity is mainly antiparallel to $\mathbf{B}$ (Figure 6h), and therefore, there is no large $\mathbf{E} \times \mathbf{B}$ force associated and the cold ions do not follow the exhaust velocity (Figure 6h). This situation may occur far from the X line or if reconnection switches off.

Nevertheless, the cold ion heating reported in this work occurs in the magnetospheric edge of the separatrix region, in association with the large $\mathbf{E}$ field gradients (related to the Hall electric field) and time variations (waves) observed in this region. The cold ion heating discussed in this work is observed upstream of the region where the pickup process operates and the $\mathbf{E}$ fields involved are different.

The $\nabla\mathbf{E}$ is shown in Figures 1i, 3e, 4i, 5g, and 6j and compared to the term qB^2/m. Despite the large uncertainties in $\nabla\mathbf{E}$ (~0.13 V/km^2 for events 1 and 3 and ~0.067 V/km^2 for events 2 and 4), we observe that the gradients of the electric field become larger in the regions where the cold ion heating is observed and exceed the value of qB^2/m, fulfilling the condition of equation (2). These large electric field gradients are in association with the large Hall $\mathbf{E}$ field, a typical feature in the magnetospheric side of asymmetric reconnection [e.g., *Khotyaintsev et al.*, 2006; *Pritchett and Mozer*, 2009]. In magnetotail reconnection, the Hall $\mathbf{E}$ field develops at both sides of the exhaust [e.g., *Drake et al.*, 2008], so the heating mechanism described here may operate in tail as well. The condition of equation (2) is clearly satisfied for events 1 and 2 (Figures 1i and 3e, the ones with

larger cold ion heating and lower cold ion density, indicating that this mechanism may play a role. The condition is marginally fulfilled for event 3 for protons (Figure 4i), where low cold ion heating was observed, and not fulfilled for event 4 (Figure 6j), where no heating is observed. The condition is easier to satisfy for heavier species, indicating that this mechanism favors the heating of heavy ions. Finally, spatial variations of **E** of scale shorter than the spacecraft separation (15 km for events 1 and 3 and 30 km for events 2 and 4) cannot be determined with the technique used. This means that the condition of equation (2) could be satisfied in very narrow regions that we cannot measure and contribute as well to the total cold ion heating.

As commented in section 1, time variations of the electric field (waves) resonant at the ion cyclotron frequency can energize particles and produce cold ion heating. We compute the perpendicular **E** field fluctuations (assuming that they correspond to time variations) in the frequency domain around f_{ci} for different time intervals for the four events discussed in section 2 (Figure 7). Each of the plotted spectra is obtained from averaging eight Fourier transforms obtained by dividing 13 s of electric field observations into eight segments with 50% overlap and using a Hamming window for each of them, where the convection **E** field has been removed (we use $\mathbf{E} + \mathbf{v}_i \times \mathbf{B}$). Black curves in Figures 7a–7d correspond to regions where no cold ion heating is observed, i.e., the magnetospheric inflow region. Blue curves correspond to time intervals when MMS observed cold ion heating. The vertical dashed lines indicate f_{ci} for protons. The ion cyclotron frequency of He^+ is significantly smaller, and we cannot reliably estimate the PSD of the **E** field at that frequency, since it would require longer observations by MMS inside the region. Differences of roughly 1 order of magnitude can be observed for the amount of **E** field energy at f_{ci} for events 1, 2, and 3 between the regions where the cold heating is observed (blue) and the magnetospheric inflow region (black). For event 4 we could not identify a region where cold ion heating is observed. Following equation (1) and assuming that at ~20% of the available energy at f_{ci} is transferred to the cold ions [*André et al.*, 1998], the heating rates inside the heating regions (blue curves) are 7 eV/s, 15 eV/s, and 15 eV/s for Figures 7a–7c, respectively. On the other hand, for the magnetospheric region where no heating is observed the same assumptions lead to heating rates of 2 eV/s, 1 eV/s, 0.5 eV/s, and 2 eV/s for Figures 7a–7d. This represents roughly 1 order of magnitude of difference between the heating regions and the regions where no heating is observed. Based on our observations, the regions where the cold ion heating occurs are confined to the vicinity of the separatrix, so the inflowing cold plasma is expected to cross this narrow region in the order of few seconds, resulting in a net heating of the order of ~100 eV [*Toledo-Redondo et al.*, 2016b]. Therefore, this mechanism can account only for part of the heating observed unless there is a trapping mechanism for cold ions inside the heating region.

Another mechanism that can be responsible for cold ion heating is lower hybrid waves (LHWs), as suggested by *Graham et al.* [2017]. LHWs are characterized by $k_\perp \gg k_{||}$ [*Karney*, 1979], and in the dense MSBL they also have $\omega \gg \Omega_{ci}$. Under these circumstances, LHW can effectively heat ions in the perpendicular direction if the perpendicular ion velocity is comparable or larger than the wave phase velocity (v_{ph}) [*McBride et al.*, 1972; *Karney*, 1978; , 1979; *Cairns and McMillan*, 2005]. Under these circumstances, parallel electron heating should be also present. We observe signatures of LHW activity in the events 2 and 3, although these observations occur in regions where cold ions from the magnetosphere and magnetosheath ion have already mixed and we cannot estimate the cold ion heating directly associated to them. This means that they cannot be the only source of cold ion heating because we observe ion heating in regions where the LHWs are not present. Nevertheless, LHWs are associated with the largest **E** field fluctuations close to the magnetopause [*Graham et al.*, 2017]. Figure 8 shows an example of a wave observation by MMS4 consistent with lower hybrid waves inside the cold ion heating region of event 3. The perpendicular total ion velocity (solid lines) and the velocity for ions below 800 eV (dashed lines) are plotted in Figure 8a. The average phase velocity of the lower hybrid wave (v_{ph}) in the green-shadowed interval is plotted using circles; see below for details on its calculation. In this interval, the cold ions mix with the magnetosheath ions (Figure 8b) and it is difficult to measure their moments independently. However, their velocity should be somewhere between the two curves of Figure 8a. Figures 8c (8d) shows the wavelet spectrogram of the **E** (**B**) field, with the lower hybrid frequency (f_{LH}) plotted on top. We observe signatures consistent with LHWs, so it is possible that they generate cold ion heating. We calculate the wave potential Φ_B of the lower hybrid waves from the local plasma conditions, as detailed in *Norgren et al.* [2012]:

$$\Phi_B = \frac{B}{qn\mu_0}\delta B_{||} \tag{4}$$

where B is the background magnetic field amplitude, δB is the high-frequency **B** fluctuations (above 10 Hz), and q and n are the electron charge and plasma density, respectively. We obtain the wave phase velocity (v_{ph})

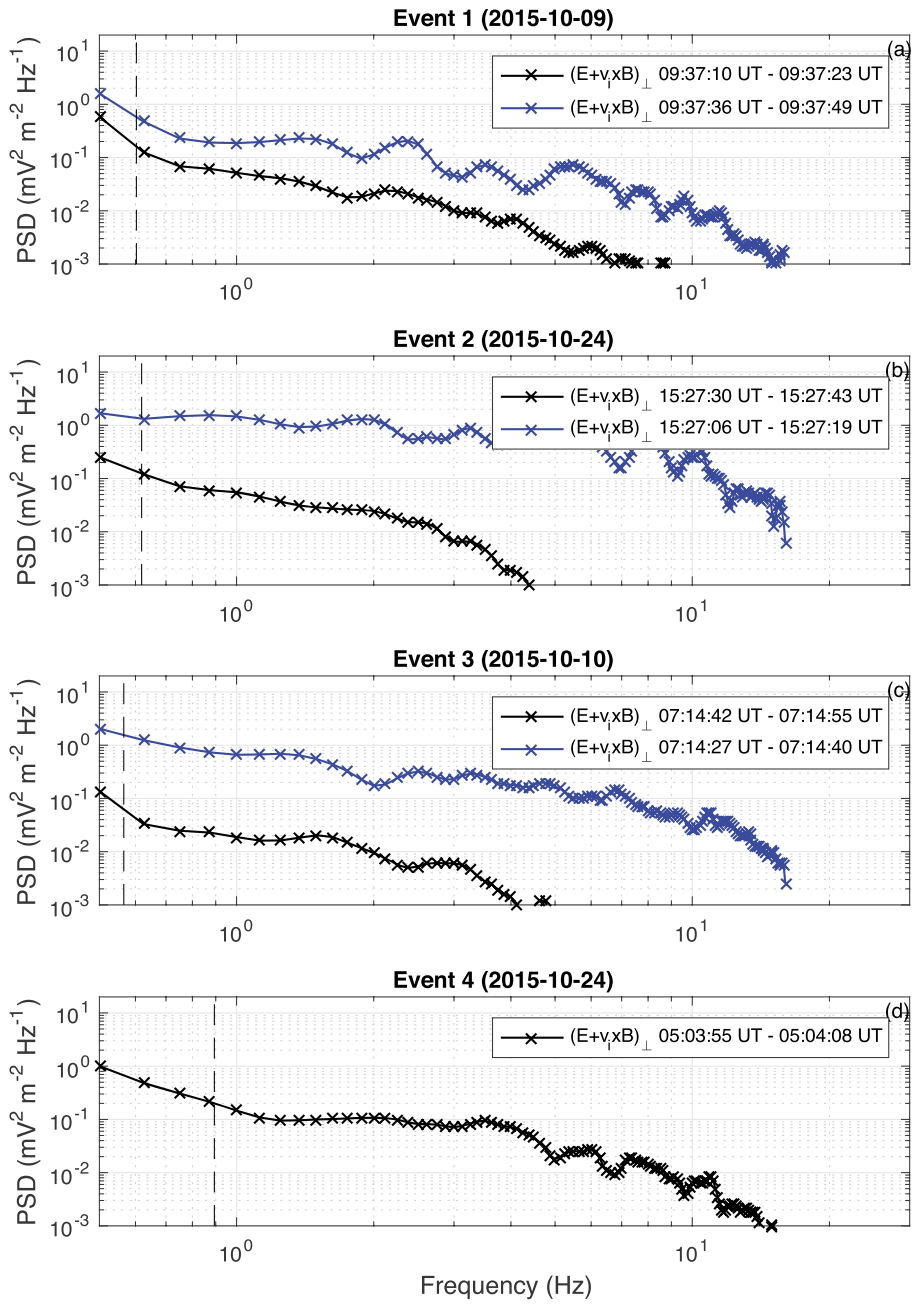

Figure 7. Fourier spectra of $(\mathbf{E} + \mathbf{v}_i \times \mathbf{B})_\perp$. Vertical dashed lines indicate the ion cyclotron frequency (f_{ci}). Blue (black) curves correspond to regions where (no) cold ion heating is observed. (a–d) The four events discussed in section 2.

by finding the best fit of the potential obtained from **E** field measurements $\Phi_E = \int \delta\mathbf{E}dt \cdot \mathbf{v}_{ph}$ to the potential (Φ_B) obtained using equation (3) [*Norgren et al.*, 2012; *Khotyaintsev et al.*, 2016; *Innocenti et al.*, 2016; *Graham et al.*, 2016, 2017]. We obtain a correlation coefficient $C = 0.88$, meaning that the phase velocity is reliable (Figure 8e).

All the mechanisms discussed for transferring energy from the fields to the particles depend on the mass of the particle. In event 3 we could obtain high-resolution moments (150 ms) for cold H^+ and He^+. The spatial scale of the heating region of He^+ is larger, consistent with its larger gyroradius. However, we could not estimate the final temperature of He^+ using high-resolution FPI measurements to check if their final temperature is larger than for protons, as one would expect from the mechanisms discussed.

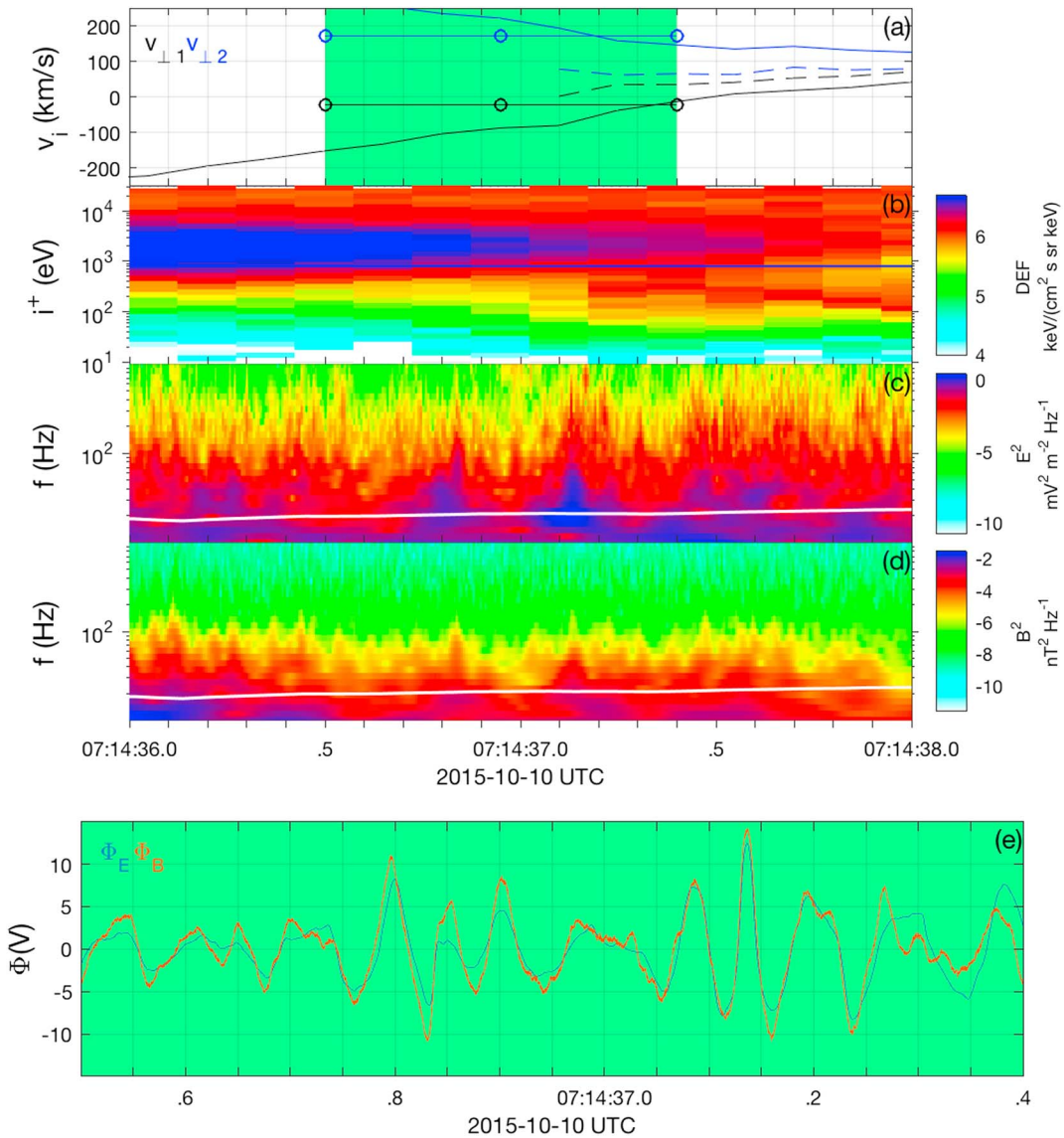

Figure 8. Detail of waves for event 3. (a) Perpendicular velocity of all ions (solid), ions below 800 eV (dashed), and estimated wave phase velocity v_{ph} (circles). (b) Omnidirectional ion DEF spectrogram. Blue line marks the cold ion threshold. (c) **E** field power wavelet spectrogram. f_{LH} is plotted in white. (d) **B** field power wavelet spectrogram. f_{LH} is plotted in white. (e) Φ_E and Φ_B of the lower hybrid waves.

4. Conclusions

We show four magnetopause crossings with reconnection jet signatures and cold plasma on the magnetospheric side. The cold plasma is heated in the inflow region, close to the separatrix region. For the events with low cold plasma density the heating is larger than for the events where the cold density was comparable to the magnetosheath density. We find a lower threshold of 10–25% of the total energy spent in ion heating, which is the dominant energy in the outflow region, goes into cold ion heating in our events, constituting a significant portion of the energy budget. We observe waves and gradients in the electric field associated with the ion heating. These spatial structures and time variations have large enough amplitudes to cause the observed ion energies. Waves essential for ion energization may occur both around the ion gyrofrequency and in the lower hybrid frequency range. For one of the events we can obtain high-resolution moments for both H^+ and He^+, and we observe that the heating region for He^+ is larger than the heating region for H^+. Overall, we find that magnetic reconnection at the subsolar magnetopause often is associated with cold ions and that heating of these ions can be an important part of the total energy budget.

Acknowledgments
We thank all the people involved in the MMS project for the high-quality data provided. We acknowledge support from the ISSI's international team *MMS and Cluster observations of magnetic reconnection*. S.T.R. holds an ESA Fellowship and acknowledges support from the Science Faculty of the European Space Astronomy Centre (ESAC). French involvement (SCM instruments) on MMS is supported by CNES, CNRS-INSIS, and CNRS-INSU. The data used in this work are available to the public in the MMS Science Data Center (https://lasp.colorado.edu/mms/sdc/public/).

References

André, M., and C. M. Cully (2012), Low-energy ions: A previously hidden solar system particle population, *Geophys. Res. Lett.*, *39*, L03101, doi:10.1029/2011GL050242.

André, M., P. Norqvist, A. Vaivads, L. Eliasson, O. Norberg, A. I. Eriksson, and B. Holback (1994), Transverse ion energization and wave emissions observed by the Freja satellite, *Geophys. Res. Lett.*, *21*(17), 1915–1918.

André, M., P. Norqvist, L. Andersson, L. Eliasson, A. I. Eriksson, L. Blomberg, R. E. Erlandson, and J. Waldemark (1998), Ion energization mechanisms at 1700 km in the auroral region, *J. Geophys. Res.*, *103*(A3), 4199–4222.

André, M., et al. (2016), Magnetic reconnection and modification of the Hall physics due to cold ions at the magnetopause, *Geophys. Res. Lett.*, *43*, 6705–6712, doi:10.1002/2016GL069665.

Angelopoulos, V. (2009), The THEMIS Mission, in *The THEMIS Mission*, edited by J. L. Burch and V. Angelopoulos, pp. 5–34, Springer, New York.

Aunai, N., G. Belmont, and R. Smets (2011), Energy budgets in collisionless magnetic reconnection: Ion heating and bulk acceleration, *Phys. Plasmas*, *18*(12), 122901, doi:10.1063/1.3664320.

Biskamp, D. (2005), *Magnetic Reconnection in Plasmas*, vol. 3, Cambridge Univ. Press, Cambridge.

Borovsky, J. E., and M. H. Denton (2006), Effect of plasmaspheric drainage plumes on solar-wind/magnetosphere coupling, *Geophys. Res. Lett.*, *33*, L20101, doi:10.1029/2006GL026519.

Borovsky, J. E., and M. H. Denton (2008), A statistical look at plasmaspheric drainage plumes, *J. Geophys. Res.*, *113*, A09221, doi:10.1029/2007JA012994.

Borovsky, J. E., M. H. Denton, R. E. Denton, V. K. Jordanova, and J. Krall (2013), Estimating the effects of ionospheric plasma on solar wind/magnetosphere coupling via mass loading of dayside reconnection: Ion-plasma-sheet oxygen, plasmaspheric drainage plumes, and the plasma cloak, *J. Geophys. Res. Space Physics*, *118*, 5695–5719, doi:10.1002/jgra.50527.

Burch, J. L., T. E. Moore, R. B. Torbert, and B. L. Giles (2015), Magnetospheric multiscale overview and science objectives, *Space Sci. Rev.*, *199*(1), 5–21, doi:10.1007/s11214-015-0164-9.

Cairns, I. H., and B. McMillan (2005), Electron acceleration by lower hybrid waves in magnetic reconnection regions, *Phys. Plasmas*, *12*(10), 102110, doi:10.1063/1.2080567.

Cassak, P., and M. Shay (2007), Scaling of asymmetric magnetic reconnection: General theory and collisional simulations, *Phys. Plasmas (1994-present)*, *14*(10), 102114.

Catapano, F., G. Zimbardo, S. Perri, A. Greco, and A. V. Artemyev (2016), Proton and heavy ion acceleration by stochastic fluctuations in the Earth's magnetotail, *Ann. Geophys.*, *34*(10), 917–926, doi:10.5194/angeo-34-917-2016.

Chang, T., G. Crew, N. Hershkowitz, J. Jasperse, J. Retterer, and J. Winningham (1986), Transverse acceleration of oxygen ions by electromagnetic ion cyclotron resonance with broad band left-hand polarized waves, *Geophys. Res. Lett.*, *13*(7), 636–639.

Chen, S.-H., and T. E. Moore (2006), Magnetospheric convection and thermal ions in the dayside outer magnetosphere, *J. Geophys. Res.*, *111*(A3), a03215, doi:10.1029/2005JA011084.

Cole, K. (1976), Effects of crossed magnetic and (spatially dependent) electric fields on charged particle motion, *Planet. Space Sci.*, *24*(5), 515–518.

Dargent, J., N. Aunai, B. Lavraud, S. Toledo-Redondo, M. Shay, P. Cassak, and K. Malakit (2017), Kinetic simulation of asymmetric magnetic reconnection with cold ions, *J. Geophys. Res. Space Physics*, *122*, 5290–5306, doi:10.1002/2016JA023831.

Darrouzet, F., J. D. Keyser, P. Décréau, F. E. Lemdani-Mazouz, and X. Vallières (2008), Statistical analysis of plasmaspheric plumes with Cluster/WHISPER observations, *Ann. Geophys.*, *26*, 2403–2417. Copernicus GmbH.

Divin, A., Y. V. Khotyaintsev, A. Vaivads, M. André, S. Toledo-Redondo, S. Markidis, and G. Lapenta (2016), Three-scale structure of diffusion region in the presence of cold ions, *J. Geophys. Res. Space Physics*, *121*, 12,001–12,013, doi:10.1002/2016JA023606.

Drake, J., M. Shay, and M. Swisdak (2008), The Hall fields and fast magnetic reconnection, *Phys. Plasmas*, *15*(4), 042306.

Drake, J., M. Swisdak, T. Phan, P. Cassak, M. Shay, S. Lepri, R. Lin, E. Quataert, and T. Zurbuchen (2009), Ion heating resulting from pickup in magnetic reconnection exhausts, *J. Geophys. Res.*, *114*, A05111, doi:10.1029/2008JA013701.

Eastwood, J., T. Phan, J. Drake, M. Shay, A. Borg, B. Lavraud, and M. Taylor (2013), Energy partition in magnetic reconnection in Earth's magnetotail, *Phys. Rev. Lett.*, *110*(22), 225001, doi:10.1103/PhysRevLett.110.225001.

Ergun, R., et al. (2016), The axial double probe and fields signal processing for the MMS mission, *Space Sci. Rev.*, *199*(1–4), 167–188.

Escoubet, C. P., M. Fehringer, and M. Goldstein (2001), Introduction: The Cluster mission, *Ann. Geophys.*, *19*(10/12), 1197–1200, doi:10.5194/angeo-19-1197-2001.

Fuselier, S. A., et al. (2016), Magnetospheric ion influence on magnetic reconnection at the duskside magnetopause, *Geophys. Res. Lett.*, *43*, 1435–1442, doi:10.1002/2015GL067358.

Graham, D. B., et al. (2016), Electron currents and heating in the ion diffusion region of asymmetric reconnection, *Geophys. Res. Lett.*, *43*, 4691–4700, doi:10.1002/2016GL068613.

Graham, D. B., et al. (2017), Lower hybrid waves in the ion diffusion and magnetospheric inflow regions, *J. Geophys. Res. Space Physics*, *122*(1), 517–533, doi:10.1002/2016JA023572.

Haerendel, G., G. Paschmann, N. Sckopke, H. Rosenbauer, and P. C. Hedgecock (1978), The frontside boundary layer of the magnetosphere and the problem of reconnection, *J. Geophys. Res.*, *83*, 3195–3216, doi:10.1029/JA083iA07p03195.

Haggerty, C., M. Shay, J. Drake, T. Phan, and C. McHugh (2015), The competition of electron and ion heating during magnetic reconnection, *Geophys. Res. Lett.*, *42*(22), 9657–9665, doi:10.1002/2015GL065961.

Hietala, H., J. Drake, T. Phan, J. Eastwood, and J. McFadden (2015), Ion temperature anisotropy across a magnetotail reconnection jet, *Geophys. Res. Lett.*, *42*, 7239–7247, doi:10.1002/2015GL065168.

Innocenti, M. E., C. Norgren, D. Newman, M. Goldman, S. Markidis, and G. Lapenta (2016), Study of electric and magnetic field fluctuations from lower hybrid drift instability waves in the with the fully kinetic, semi-implicit, adaptive multi level multi domain method, *Phys. Plasmas*, *23*(5), 052902.

Karney, C. F. (1978), Stochastic ion heating by a lower hybrid wave, *Phys. Fluids*, *21*(9), 1584–1599.

Karney, C. F. (1979), Stochastic ion heating by a lower hybrid wave: II, *Phys. Fluids*, *22*(11), 2188–2209.

Khotyaintsev, Y. V., A. Vaivads, A. Retinò, M. André, C. J. Owen, and H. Nilsson (2006), Formation of inner structure of a reconnection separatrix region, *Phys. Rev. Lett.*, *97*(20), 205003.

Khotyaintsev, Y. V., et al. (2016), Electron jet of asymmetric reconnection, *Geophys. Res. Lett.*, *43*, 5571–5580, doi:10.1002/2016GL069064.

Le Contel, O., et al. (2016), The search-coil magnetometer for MMS, *Space Sci. Rev.*, *199*(1–4), 257–282.

Lee, S. H., H. Zhang, Q.-G. Zong, A. Otto, H. Rème, and E. Liebert (2016), A statistical study of plasmaspheric plumes and ionospheric outflows observed at the dayside magnetopause, *J. Geophys. Res. Space Physics*, *121*, 492–506, doi:10.1002/2015JA021540.

Lindqvist, P.-A., et al. (2014), The spin-plane double probe electric field instrument for MMS, *Space Sci. Rev.*, *199*(1–4), 137–165, doi:10.1007/s11214-014-0116-9.
Lindstedt, T., Y. V. Khotyaintsev, A. Vaivads, M. André, H. Nilsson, and M. Waara (2010), Oxygen energization by localized perpendicular electric fields at the cusp boundary, *Geophys. Res. Lett.*, *37*, L09103, doi:10.1029/2010GL043117.
McBride, J. B., E. Ott, J. P. Boris, and J. H. Orens (1972), Theory and simulation of turbulent heating by the modified two-stream instability, *Phys. Fluids*, *15*(12), 2367–2383.
Norgren, C., A. Vaivads, Y. V. Khotyaintsev, and M. André (2012), Lower hybrid drift waves: Space observations, *Phys. Rev. Lett.*, *109*(5), 055001.
Olsen, R. C. (1982), The hidden ion population of the magnetosphere, *J. Geophys. Res.*, *87*(A5), 3481–3488.
Phan, T., J. Drake, M. Shay, J. Gosling, G. Paschmann, J. Eastwood, M. Oieroset, M. Fujimoto, and V. Angelopoulos (2014), Ion bulk heating in magnetic reconnection exhausts at Earth's magnetopause: Dependence on the inflow Alfvén speed and magnetic shear angle, *Geophys. Res. Lett.*, *41*, 7002–7010, doi:10.1002/2014GL061547.
Pollock, C., et al. (2016), Fast plasma investigation for Magnetospheric Multiscale, *Space Sci. Rev.*, *199*(1–4), 331–406.
Priest, E., and T. Forbes (2000), Book review: Magnetic reconnection/Cambridge U Press, 2000, *Irish Astronomical J.*, *27*, 235.
Pritchett, P. (2008), Collisionless magnetic reconnection in an asymmetric current sheet, *J. Geophys. Res.*, *113*, A06210, doi:10.1029/2007JA012930.
Pritchett, P., and F. Mozer (2009), Asymmetric magnetic reconnection in the presence of a guide field, *J. Geophys. Res.*, *114*, A11210, doi:10.1029/2009JA014343.
Russell, C., et al. (2014), The magnetospheric multiscale magnetometers, *Space Sci. Rev.*, *199*(1), 189–256.
Sauvaud, J.-A., et al. (2001), Intermittent thermal plasma acceleration linked to sporadic motions of the magnetopause, first Cluster results, *Ann. Geophys.*, *19*, 1523–1532.
Sonnerup, B. U. (1974), Magnetopause reconnection rate, *J. Geophys. Res.*, *79*(10), 1546–1549.
Stasiewicz, K., R. Lundin, and G. Marklund (2000), Stochastic ion heating by orbit chaotization on electrostatic waves and nonlinear structures, *Phys. Scr.*, *2000*(T84), 60.
Stasiewicz, K., S. Markidis, B. Eliasson, M. Strumik, and M. Yamauchi (2013), Acceleration of solar wind ions to 1 Mev by electromagnetic structures upstream of the Earth's bow shock, *EPL (Europhysics Letters)*, *102*(4), 49001.
Swisdak, M., and F. Drake (2007), Orientation of the reconnection X-line, *Geophys. Res. Lett.*, *34*, L11106, doi:10.1029/2007GL029815.
Toledo-Redondo, S., A. Vaivads, M. André, and Y. V. Khotyaintsev (2015), Modification of the Hall physics in magnetic reconnection due to cold ions at the Earth's magnetopause, *Geophys. Res. Lett.*, *42*, 6146–6154, doi:10.1002/2015GL065129.
Toledo-Redondo, S., et al. (2016a), Cold ion demagnetization near the X-line of magnetic reconnection, *Geophys. Res. Lett.*, *43*, 6759–6767, doi:10.1002/2016GL069877.
Toledo-Redondo, S., M. André, A. Vaivads, Y. V. Khotyaintsev, B. Lavraud, D. Graham, A. Divin, and N. Aunai (2016b), Cold ion heating at the dayside magnetopause during magnetic reconnection, *Geophys. Res. Lett.*, *43*, 58–66, doi:10.1002/2015GL067187.
Walsh, B., D. Sibeck, Y. Nishimura, and V. Angelopoulos (2013), Statistical analysis of the plasmaspheric plume at the magnetopause, *J. Geophys. Res. Space Physics*, *118*, 4844–4851, doi:10.1002/jgra.50458.
Walsh, B., T. Phan, D. Sibeck, and V. Souza (2014), The plasmaspheric plume and magnetopause reconnection, *Geophys. Res. Lett.*, *41*, 223–228, doi:10.1002/2013GL05880.
Wu, C. S., Y. Li, J. K. Chao, P. H. Yoon, and L. C. Lee (1998), Solar energetic ions created in a reconnection layer by Alfvén wave pickup, *Astrophysical J.*, *495*(2), 951–956.
Young, D., et al. (2016), Hot plasma composition analyzer for the Magnetospheric Multiscale mission, *Space Sci. Rev.*, *199*(1–4), 407–470.